Biodegradable Zn–Sr alloy for bone regeneration in rat femoral condyle defect model: In vitro and in vivo studies

Bo Jia [a,c,1], Hongtao Yang [b,d,1], Zechuan Zhang [b,1], Xinhua Qu [e], Xiufeng Jia [f], Qiang Wu [a], Yu Han [a], Yufeng Zheng [b,**], Kerong Dai [a,*]

[a] *Department of Orthopaedic Surgery, Shanghai Key Laboratory of Orthopaedic Implants, Shanghai Ninth People's Hospital, Shanghai Jiaotong University, School of Medicine, Shanghai, 200011, China*
[b] *Department of Materials Science and Engineering, College of Engineering, Peking University, Beijing, 100871, China*
[c] *Department of Orthopedics, Shanghai General Hospital, Shanghai Jiao Tong University School of Medicine, Shanghai, 200080, China*
[d] *Department of Materials Science and Engineering, The Ohio State University, Columbus, OH, 43210, United States*
[e] *Department of Bone and Joint Surgery, Renji Hospital, School of Medicine, Shanghai Jiao Tong University, Shanghai, 200127, China*
[f] *Department of Orthopaedic Surgery, Wudi People's Hospital, Binzhou, 251900, China*

ARTICLE INFO

ABSTRACT

Bone defects are commonly caused by severe trauma, malignant tumors, or congenital diseases and remain among the toughest clinical problems faced by orthopedic surgeons, especially when of critical size. Biodegradable zinc-based metals have recently gained popularity for their desirable biocompatibility, suitable degradation rate, and favorable osteogenesis-promoting properties. The biphasic activity of Sr promotes osteogenesis and inhibits osteoclastogenesis, which imparts Zn–Sr alloys with the ideal theoretical osteogenic properties. Herein, a biodegradable Zn–Sr binary alloy system was fabricated. The cytocompatibility and osteogenesis of the Zn–Sr alloys were significantly better than those of pure Zn in MC3T3-E1 cells. RNA-sequencing illustrated that the Zn-0.8Sr alloy promoted osteogenesis by activating the wnt/β-catenin, PI3K/Akt, and MAPK/Erk signaling pathways. Furthermore, rat femoral condyle defects were repaired using Zn-0.8Sr alloy scaffolds, with pure Ti as a control. The scaffold-bone integration and bone ingrowth confirmed the favorable in vivo repair properties of the Zn–Sr alloy, which was verified to offer satisfactory biosafety based on the hematoxylin-eosin (H&E) staining and ion concentration testing of important organs. The Zn-0.8Sr alloy was identified as an ideal bone repair material candidate, especially for application in critical-sized defects on load-bearing sites due to its favorable biocompatibility and osteogenic properties in vitro and in vivo.

1. Introduction

Bone tissue exhibits a relatively strong regeneration and repair ability [1]. However, the bone defects typically caused by severe trauma, malignant tumors, or congenital diseases may require bone grafts to promote complete repair [2]. Over 2 million fracture patients require bone graft treatment in the United States per year, where the associated medical expenses are estimated to be as high as 3.9 billion USD [3]. China has over 10 million patients with physical dysfunction due to bone defects [4]. Furthermore, the increase in modern human life expectancy has led to an increase the skeletal disease incidence among the elderly (e.g., bone fractures, rheumatoid arthritis, osteoporosis and bone metastases) [5]. These ailments and diseases often affect the load-bearing portion of the skeleton, but there is currently no gold standard for the repair of bone defects in the load-bearing portions of a skeleton.

Typical bone repair materials currently used in clinical applications include biological bones (autologous bones, allogeneic bones, and xenogeneic bones), bioceramics (hydroxyapatite (HA), beta-tricalcium phosphate (beta-TCP), and calcium phosphate (CaP)), synthetic polymers (poly(lactic acid) (PLA), poly(caprolactone) (PCL), poly(glycolic acid) (PGA), and poly(lactide-co-glycolide) (PLGA)), and biomedical

---

metals (titanium, stainless steel, and tantalum) [6]. Autologous bone exhibits good osteogenesis, osteoinduction, and osteoconduction characteristics and is a benchmark for bone repair materials [7]. However, autologous bone grafts may cause pain, discomfort, and the formation of secondary bone defects at the donor site. Additional problems associated with autologous bone grafts include a limited donor bone mass and possible shape mismatch with the defect site [8]. However, the alternative bone repair materials have drawbacks too. Bioceramics and synthetic polymers do not offer sufficient mechanical support for bone defects on load-bearing sites [9], while biomedical metals offer sufficient mechanical properties but lack osteogenic activity. Furthermore, the elastic modulus of the biomedical metals is much higher than cortical bone and can cause stress shielding or bone mass loss [10]. These metals are not degradable, which leads to difficult removal, even through secondary surgery [11]. Although optimization of these materials has been achieved using coating and compositing [12,13], clinical applications rely on further fundamental improvements of the underlying materials. These novel bone repair materials must be capable of adapting to the requirements of bone repair, namely, (1) satisfactory biocompatibility; (2) sufficient mechanical properties for bone injury repair and lower elastic modulus; (3) an appropriate degradation rate to match the bone repair process; and (4) facilitating biological functions. These biological functions include osteogenicity, which promotes the differentiation of osteoprogenitor cells into osteoblasts to increase new bone formation; osteoinductivity, which provides relevant growth factors, including bone morphogenetic proteins (BMPs), or enhances their function; osteoconductivity, which provides an absorbable or nonabsorbable scaffold in the new bone ingrowth space [14]; and angiogenesis, which provides new blood vessels for bone regeneration [15]. Considering the importance of these functions and processes, biodegradable metallic materials that promote these biological functions are promising candidates expected to satisfy these needs.

Biodegradable Zn-based metals have attracted widespread attention [16–18]. Zn plays an important role in bone formation and mineralization [19] by inhibiting bone resorption by osteoclasts and promoting bone formation by osteoblasts to increase bone mass [20]. Furthermore, studies have indicated that Zn could promote new bone formation by promoting osteoblast proliferation [21], up-regulating alkaline phosphatase (ALP) activity [22], promoting collagen synthesis [23], and activating the expression of Runx-2 (runt-related transcription factor 2) and downstream genes [24–26]. Biodegradable zinc-based materials show promise for bone repair applications, but the poor material properties and biocompatibility of pure Zn must be addressed [27]. The current authors conducted a previous study in which Zn-HA [28] and Zn–Mg composites were found to exhibit improved biocompatibility in comparison with pure Zn, thereby promoting in vivo osseointegration [29]. However, these composite materials did not meet all of the prescribed requirements for a bone repairing material, specifically the mechanical properties and biofunctionality. Thereafter, a series of binary Zn-X (X = Mg [30], Ca [31], Sr, Li, Mn [32], Cu, and Ag [33]) alloys were manufactured in an attempt to improve the mechanical properties and biocompatibility of pure Zn, where the Zn–Sr alloys exhibited the best osteogenic properties. This superior performance was attributed to the biphasic activity of Sr, which promoted osteogenesis and inhibited osteoclastogenesis [34]. Therefore, biodegradable Zn–Sr alloys with satisfactory osteogenic activities are expected to become viable candidates for bone repair. The previous studies were limited to material properties and simple bone implantation, and the osteogenic activity and biological mechanisms of Zn–Sr alloys were not comprehensively evaluated. This study aimed to evaluate a series of binary Zn-xSr alloys (x = 0.1, 0.4, and 0.8 wt %) based on their osteogenic activities and biological mechanisms. Furthermore, the feasibility of Zn–Sr alloys as bone repair material was investigated based on a partial load-bearing site bone defect in rat femoral condyle defect models.

2. Materials and methods

2.1. The preparation of materials and extracts

2.1.1. Material preparation

Zn–Sr alloys were prepared from high purity Zn (99.99%) and Sr (99%) raw materials. Mass percentages of 0, 0.1, 0.4, and 0.8 wt % Sr were used, where the samples were denoted as pure Zn, Zn-0.1Sr, Zn-0.4Sr, and Zn-0.8Sr, respectively. The nominal and actual compositions of pure Zn and the Zn–Sr alloys are presented in Table S1. The Zn alloys were homogenized at 350 °C for 48h before extrusion at a ratio of 36 at 1 mm/s and quenched in water. The final diameter of the extruded bars was 10 mm. The pure Zn and Zn–Sr alloys were cut into disc-shaped (∅10 × 1 mm) and cylindrical (∅3 × 4 mm) samples. The samples were mechanically polished to a mesh of 2000, cleaned under ultrasound in acetone and ethanol, and dried at room temperature. Samples were sterilized using ethylene oxide before performing the cytotoxicity and animal experiments.

2.1.2. Microstructure characterization

Samples were ground to a 5000 grit surface, polished with 0.1 μm diamond paste, and cleaned in distilled water. The samples were etched with a 4% HNO3/alcohol solution for 5–10 s. A scanning electron microscope (SEM; Hitachi S-4800, Japan) equipped with energy dispersive spectrometry (EDS) was used for microstructural observations and compositional analysis. Phase composition was investigated using an X-ray diffractometer (XRD, Rigaku DMAX 2400, Japan) with a CuKα source was operated at 40 kV and 100 mA in a scanning range of 20°–90° at a scan rate of 2°/min with 0.02° intervals.

2.1.3. Mechanical tests

Samples for the tensile and compressive tests were prepared according to ASTM-E8-04a and ASTM-E9-89 standards, respectively. A universal material test machine (Instron 5969, USA) was used at room temperature, where displacement rates of $1 \times 10-4$/s and $2 \times 10-4$/s were used for the tensile and the compressive tests, respectively. The yield strength was the stress at which 0.2% plastic deformation occurred. The ultimate compressive strength was the maximum stress applied before 50% compressive strain. Microhardness testing was performed using a microhardness tester (Shimadzu HMV-2T) to measure Vickers hardness with a 0.1 kN loading force and 15 s dwell time. The test was conducted five times for each sample group to determine a mean value.

2.1.4. Electrochemical test

Electrochemical tests were conducted via an electrochemical working station (Autolab, Metrohm, Switzerland) at 37 °C in a simulated body fluid (SBF) solution (NaCl 8.035 g/L, NaHCO3 0.355 g/L, KCl 0.25 g/L, K2HPO4·3H2O 0.231 g/L, MgCl2·6H2O 0.311 g/L, HCl (36–38%) 39 mL/L, CaCl2 0.292 g/L, Na2SO4 0.072 g/L, Tris 6.118 g/L, pH 7.4). A three-electrode cell equipped with a platinum counter electrode and a saturated calomel electrode (SCE) was used as the reference electrode. The open-circuit potential (OCP) was monitored for each sample for 5400 s. Electrochemical impedance spectroscopy (EIS) was conducted with a 10 mV perturbation in a frequency range of 105 Hz to 10-2 Hz. Potentiodynamic polarization was conducted at a scan rate of 1 mV/s from −500 mV to 500 mV (vs. OCP) in a test area of 0.2826 cm^2. The corrosion potential (Ecorr) and corrosion current density (icorr) were interpolated by linear fit and Tafel extrapolation. The tests were conducted five times for each sample group to determine mean values.

2.1.5. Immersion test

Samples were immersed in SBF solutions at 37 °C for 30 days at a solution-to-area ratio of 20 mL/cm2, as stipulated by the ASTM-G31-72 standard. The solution was replaced every 48 h. The samples were rinsed with distilled water, dried in air and a 200 g/L CrO3 solution was used to

remove the corrosion products. The corrosion morphology before and after the removal of the corrosion products was observed by SEM. The corrosion rates were calculated based on weight loss according to the equation: $C = \Delta m / \rho At$, where C is the corrosion rate in mm/year, Δm is the weight loss, ρ is the density of the material, A is the initial implant surface area, and t is the implantation time. The test was conducted a minimum of five times for each sample group to determine an average value.

2.1.6. Preparation of Zn–Sr alloys extracts

Zn–Sr alloys extracts were prepared according to the ISO 10993 standard. The pure Zn and Zn–Sr alloys metal discs were soaked in a prepared alpha minimum essential medium (α-MEM) cell culture medium at a specific surface area ratio of 1.25 mL/cm2 and incubated in a cell culture incubator (37 °C, 5% CO2 and saturated humidity). The alloy extracts were collected after 24 h and filtered using a sterile filter. Samples were stored at 4 °C for no more than 3 days before use.

2.2. In vitro cell experiments

Mouse osteogenic precursor cells (MC3T3-E1, ATCC CRL-2594™) were used to evaluate the cytocompatibility and osteogenic properties of pure Zn and the Zn–Sr alloys, and to explore the potential biological mechanisms.

2.2.1. Cell culture

MC3T3-E1 cells were resuscitated and cultured in an α-MEM (supplemented with 10% FBS, 1% penicillin (100 U/mL), and streptomycin sulfate (100 mg/mL) (Gibco, Grand Island, NY)) culture medium in a cell culture incubator (37 °C, 5% CO2 and saturated humidity). The cells were observed using a microscope. Once 90% of the MC3T3-E1 cells were confluent, the cultures were digested with 0.25% trypsin and centrifuged at 300 G for 5 min. The cell pellet was collected and resuspended. A Cell Counting Kit-8 (CCK-8, Dojindo Molecular Technology, Japan) was used to measure the cell concentration and standardized to evaluate the cellular proliferation of the MC3T3-E1 cells.

2.2.2. Cell proliferation activity

The concentration of the resuspended MC3T3-E1 cells was adjusted and equal amounts of cells were seeded in a 96-well plate (100 µl per well). The plate was incubated in a cell culture incubator (37 °C, 5% CO2, and saturated humidity) for 2–4 h. The cells became attached to the wells and the culture medium was replaced with the pure Zn, Zn-0.1Sr, Zn-0.4Sr, and Zn-0.8Sr extracts, where the ion concentrations of the pure Zn and Zn–Sr alloy extracts are shown in Table S2. Pure α-MEM culture medium was used as a control. Five wells were assigned to each sample group and were tested at 1, 3, 5, and 7 days in co-culture.

The influence of the Zn–Sr alloy extracts on the cellular morphology was evaluated by staining the co-cultured MC3T3-E1 cells using a Live/Dead cell staining procedure and a cytoskeletal staining procedure (cytoskeleton labeled with phalloidin and nuclei labeled with DAPI). The stained cells were observed using confocal laser scanning microscopy (CLSM, Leica TCS SP2; Leica Microsystems, Heidelberg, Germany) to assess cell survival and spreading morphology.

2.2.3. ALP activity and ALP staining

The resuspended MC3T3-E1 cells (adjusted concentration) were seeded in a six-well plate (2 × 104 cells per mL, 2 mL per well) and incubated in a cell culture incubator (37 °C, 5% CO2 and saturated humidity) for 2–4 h. The attached cells were observed under a microscope. When 80% of the cells were confluent, the culture medium was replaced with an osteogenic medium prepared from the pure Zn, Zn-0.1Sr, Zn-0.4Sr, and Zn-0.8Sr extracts to induce differentiation for 7 and 14 days. Three wells were used per group, and the medium was replaced every 48 h. The osteogenic medium was discarded, and the wells were gently washed three times with PBS. The ALP activity of the

MC3T3-E1 cells differentiated for 7 and 14 days was quantitatively analyzed according to the ALP quantitative analysis kit instructions (Nanjing Jiancheng Bioengineering Institute, China). The MC3T3-E1 cells differentiated for 7 and 14 days were stained using the ALP staining kit (Shanghai Hongqiao Le Xiang Institute of Biomedical Products, Shanghai, China) and digital photographs.

2.2.4. Osteogenic-related gene expression of the MC3T3-E1 cells

The osteogenic-related gene expression of the MC3T3-E1 cells was detected using real-time quantitative polymerase chain reaction (qt-PCR). The resuspended MC3T3-E1 cells (adjusted concentration) were seeded in a six-well plate (2 × 104 cells per mL, 2 mL per well) and incubated in a cell culture incubator (37 °C, 5% CO2 and saturated humidity) for 2–4 h. The attached cells were observed under a microscope. When 80% of the cells were confluent, osteogenic differentiation was induced. An osteogenic medium was prepared based on the ALP activity results, where one- and two-fold dilutions of the Zn–Sr alloy extract were used to induce cell differentiation for 10 days. The cells were observed daily and the culture medium was replaced every 48 h. The total RNA was extracted using an RNeasy mini kit (Qiagen, Germany). β-actin was used as an internal reference to measure the mRNA expression of the marker genes (ALP, OCN, RunX-2, and Col I) of the MC3T3-E1 cells using qt-PCR. The primer sequences are shown in Table S3. A reverse transcription kit (SuperScriptTM III Reverse Transcriptase) was used to reverse 1 mg RNA. SYBR Premix Ex Taq II (2 ×) was used as PCR reagents to perform qt-PCR assays with an ABI 7500 Fast machine (Applied Biosystems, Courtaboeuf, France). The results were calculated using the delta-delta Ct method (2-$\triangle\triangle$Ct) method.

2.3. Biological function of Zn-0.8Sr alloy (RNA sequencing and western-blot)

The experimental results indicated the superior performance of the Zn-0.8Sr alloy, which was selected for the further evaluation of the mechanisms through which the Zn-0.8Sr alloy promotes cell proliferation and osteogenic differentiation.

The cells were cultured according to the methods described in Section 2.2.1. A two-fold dilution of the Zn-0.8Sr alloy extract was used to induce osteogenic differentiation of the MC3T3-E1 cells for 12 days. A blank osteogenic medium (no Zn-0.8Sr alloy extract) was used as a control. RNA sequencing (Shanghai OE Biotech Co., Ltd) was used to detect the expression of all mRNA genes present in the MC3T3-E1 cells. The differential genes were screened via transcript-level quantification, and differential transcripts with p-values below 0.05 and two-fold greater expression were selected. Gene Ontology (GO) and Kyoto Encyclopedia of Genes and Genomes (KEGG) enrichment analyses were performed to determine the biological functions of the genes and/or the pathways influenced by the selected differential transcripts. The genes related to osteogenic activity were selected and verified by qt-PCR using the 2-$\triangle\triangle$Ct analytical method, as described in Section 2.2.4. Genes related to bone mineralization (Ibsp, Pth1r, Mmp13, Fgfr3, Pthlh, Axin2, and Aspn), bone morphogenesis (Sfrp2, Actn3, Cyp26b1, and Pappa2), ossification (Rassf2, Clec11a, Pth1r, Kazald1, Fgfr2, Fzd9, Chrdl1, Bmp4, and Mmp9), and bone remodeling (Lrp5, Lepr, and Fgfr3) were identified. The primer sequences are shown in Table S4.

The quantitative analysis of expression levels of osteogenic related genes revealed that the Zn-0.8Sr alloy up-regulated the expression levels of Ibsp (integrin-binding sialoprotein), Mmp13 (matrix metallopeptidase 13), Kazald1 (Kazal-type serine peptidase inhibitor domain 1), and Fgfr3 (fibroblast growth factor receptor 3) in the MC3T3-E1 cells. Ibsp, Mmp13, Kazald1, and Fgfr3 are components in the PI3K/AKT signaling pathway, while the latter three also participate in the MAPK/Erk pathway. Both signaling pathways play a crucial role in bone repair. Furthermore, the expression levels of Lrp5 (low-density lipoprotein receptor-related protein 5) and Fzd9 (frizzled class receptor 9) were also up-regulated, which can activate the wnt/β-catenin signaling

pathway that participates throughout the bone repair process. Therefore, the activation of the PI3K/AKT, MAPK/Erk, and wnt/β-catenin signaling pathways were evaluated in the osteogenic differentiation of the MC3T3-E1 cells. The expression profiles of the key proteins in each pathway, i.e., Akt and p-Akt in PI3K/AKT, Erk in MAPK/Erk, and β-catenin and Wnt 3a in Wnt/β-catenin, were evaluated by Western blot. Subsequently, the expression levels of downstream osteogenic proteins (ALP, COL I, OCN, and Runx-2) were also evaluated by Western blot.

2.4. In vivo testing of Zn–Sr alloys

2.4.1. Implant selection and preparation

The Zn-0.8Sr alloy was selected for the in vivo evaluation of osteogenic activity and biosafety based on the in vitro results. Pure Zn was not used as a control because previous studies found that pure Zn was not suitable for bone repair after delayed osteointegration, poor bone regeneration, and obvious inflammatory were observed when pure Zn rods were implanted into rat femoral condyles [28,33,35]. Therefore, pure Ti is a metallic material used for clinical repair of large bone defects and was chosen as the control. Porous cylindrical Zn-0.8Sr alloy and pure Ti scaffolds with a diameter of 3 mm and height of 4 mm were used. Holes with a diameter of 0.5 mm were formed in the cylindrical samples using laser cauterization (TruLaser Tube 5000 fiber, Germany). Schematic diagrams and the three-dimensional reconstructed images of the implants are shown in Fig. S1. The porosity of scaffolds was shown in Table S5.

2.4.2. Surgical procedure

All animal operations and experiments were approved by the Animal Ethics Committee of Shanghai Rat & Mouse Biotech Co., Ltd. A cylindrical bone defect repair model for rat lateral femoral condyle was established. A total of 30 male rats aged 12 weeks (average weight: 296 g $\pm$ 25.6 g) were used. The surgery was performed under sterile conditions. The rats were anesthetized with an intraperitoneal injection of ketamine (10 mg/kg, Shanghai Ziyuan Pharmaceutical Co. Ltd, Shanghai, China) and 2% xylazine (10 mg/kg, Shanghai Ziyuan Pharmaceutical Co. Ltd, Shanghai, China). Buprenorphine (Temgesic, Reckitt & Cloman, Hull, UK) was injected subcutaneously for postoperative analgesia. The right hind limb was shaved, and the knee joint was fixed at maximum extension. A 15 mm longitudinal incision was made lateral to the patellar ligament to expose the lateral femoral condyle. A cylindrical bone defect 3 mm in diameter and 4 mm in depth was formed via drilling with a 3 mm drill bit and the broken bone chips were washed away with saline. A Zn-0.8Sr alloy or pure Ti scaffold was implanted. The surgery site was rinsed with normal saline and the incision was sutured layer by layer. The rats were euthanized after 4, 8, and 12 weeks to collect the femurs. There were two operation groups, namely, the pure Ti control group with a pure Ti porous scaffold to repair the bone defect and the Zn-0.8Sr alloy experimental group with a Zn-0.8Sr alloy porous scaffold. A total of 15 rats were used per group (pure Ti and Zn-0.8Sr alloy), where give rats were euthanized to collect the femurs at 4, 8, and 12 weeks (i.e., five rats per time duration per group).

2.4.3. In vivo osteogenic properties of Zn–Sr alloy

The right femur of each euthanized rat was completely removed and fixed with 4% paraformaldehyde. The distal femur and femoral condyle were scanned using micro-computed tomography (micro-CT) (Scanco Micro-ct100, Switzerland). The detailed scanning parameters are provided in Table S6. After the scan was completed, three-dimensional reconstructions were performed using Scanco μ100 Evaluation software, with a 1 mm diameter area around the implant as the region of interest (ROI). Osteogenesis indices, including BMD (Bone Mineral Density), BV/TV (Bone volume fraction), Tb.N (Trabecular Numbers), Tb.Sp (Trabecular Separation), and Tb.Th (Trabecular Thickness), were quantitatively analyzed in the ROIs. The osteogenic activity and degradation behavior of the Zn-0.8Sr alloys in vivo were evaluated based on the micro-CT results.

2.4.4. Histomorphometric evaluation

Hard tissue staining was conducted on the rat femurs fixed with 4% paraformaldehyde (n = 30). The femurs were rinsed in water, dehydrated in ethanol, cleaned in xylene, and placed in methyl methacrylate. Each femur was cut along the longitudinal portion (vertical to the implant in the femur condyle) to give four to five sections per femur. The sections were ground and polished to a thickness of 100 μm. Van Gieson, toluidine blue, and paragon staining were performed, and the samples were examined and imaged using a high-quality microscope (Olympus CKX41, Olympus Co. Ltd., Tokyo, Japan) and an automatic digital slide scanner (Pannoramic MIDI, 3D HISTECH, Budapest, Hungary). Full-view images areas (20 ×), low-magnification images (50 ×), and high-magnification images (100 ×) of the bone defect were acquired. The full-view images of the Van Gieson stained samples were used during histomorphometric analysis. A concentric circle (diameter = 4 mm) around the scaffolds was defined as the region of interest (ROI). Image-pro plus 6.0 software (Media Cybernetics, Inc., Rockville, MD, USA) was used to conduct semi-quantitative analyses.

2.4.5. Cross-sectional analysis

One section of each femur was selected for cross-sectional analysis and was coated with a thin layer of gold to improve the conductivity of the surface. The cross-section of each sample was observed using an SEM (Hitachi S-4800, Japan) equipped with EDS. Images of the samples were acquired with SEM and the distribution of the typical elements was detected by EDS mapping.

2.4.6. General condition of animals and in vivo biosafety

The general post-surgical condition of each rat, including body temperature, body weight, and wound healing, was observed daily. Postoperative cardiac blood samples were randomly collected at 12 weeks from rats in the pure Ti control group and the Zn-0.8Sr alloy experimental group. The Zn2+ and Sr2+ serum concentrations in the blood samples were measured using ICP-mass spectrometry (ICP-MS, NexION 300Â, USA). The postoperative Zn2+ and Sr2+ concentrations in the rats' organs (heart, liver, spleen, lung, and kidney) were determined at 12 weeks, where samples were randomly collected from the pure Ti control group and the Zn-0.8Sr experimental group and measured using ICP-MS. The sampled organ tissues were fixed, embedded, and stained with hematoxylin-eosin (H&E) to reveal if pathological changes had occurred.

2.5. Data analysis

Data analysis was performed using the SPSS 25.0 statistical software (SPSS Inc. Chicago, USA). The quantitative data were presented as mean value $\pm$ standard deviation (SD). Data were analyzed using the independent sample *t*-test and one-way analysis of variance (ANOVA). The difference was considered to be statistically significant if either $p < 0.05$ (indicated as *) or $p < 0.01$ (indicated as **).

3. Results

3.1. Materials characterization

3.1.1. Microstructure and mechanical properties

In Fig. 1a, pure Zn showed a grain size of 4.84 $\pm$ 0.95 μm (Table S7), which initially increased slightly after adding 0.1 wt% Sr but then decreased with the increasing Sr content. The volume of the intermetallic phase increased with the increasing Sr concentration. This phase was identified as SrZn13 using X-ray diffraction and EDS analysis (Fig. S2), and the intensity of the characteristic SrZn13 peaks was higher at increased Sr concentrations. The mechanical properties of the as-extruded Zn–Sr alloys revealed that there was no strengthening of the
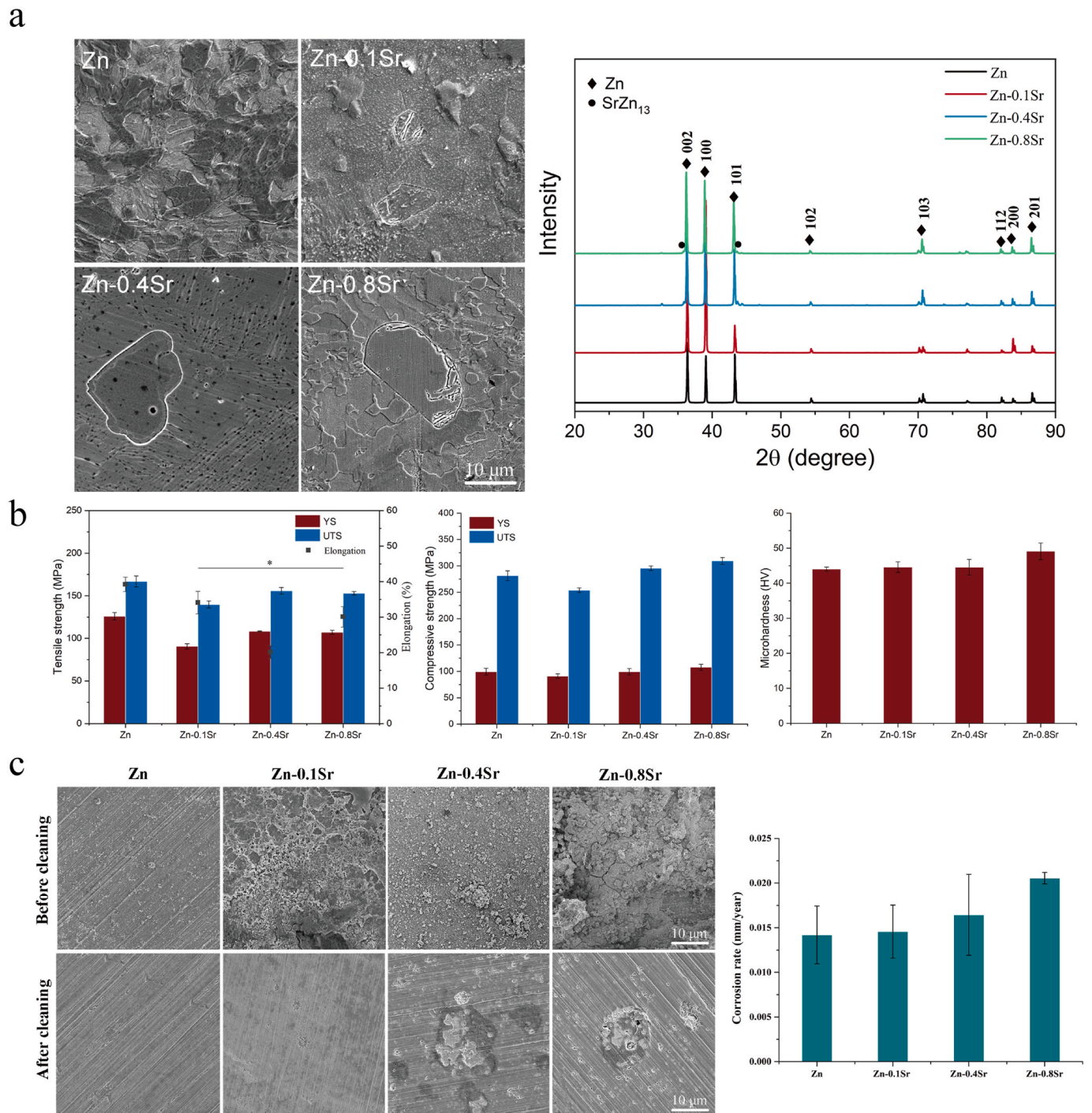
Fig. 1. Material characterization of Zn–Sr alloys. (a) Microstructure and intermetallic phase of pure Zn and the Zn–Sr alloys. (b) Mechanical properties of pure Zn and the as-extruded Zn–Sr alloys. (c) Corrosion morphology after immersion in SBF solution for 30 days.

Zn matrix when Sr was added up to 0.8 wt% (Fig. 1b), while the elongation to failure decreased as Zn was replaced (Fig. S3). Similar phenomena were observed for the compressive strength and microhardness.

3.1.2. In vitro corrosion behavior

Polarization curves and electrochemical impedance spectra (EIS) were acquired to evaluate the corrosion behavior of Zn–Sr alloys (Fig. S4). The calculated electrochemical parameters are shown in Table S8. The corrosion potential tended to shift negatively with increasing Sr concentration, while the corrosion current density exhibited a significant increase. Numerous reactions were observed in

the cathode region of the Zn–Sr alloy polarization curves, which is a notable difference from the pure Zn samples. Moreover, the Zn–Sr alloys exhibited lower corrosion resistance than pure Zn, which was validated by the decreased radius of the impedance semicircle when Sr concentration increased. The corrosion morphology of the experimental samples after immersion in SBF solution for 30 days is shown in Fig. 1c, where a large amount of corrosion products and precipitates covered the surface of the Zn–Sr alloys. However, this was not observed in the pure Zn samples. The corrosion products were removed to reveal an intact Zn surface. Corrosion pits were observed on the surface of the Zn–Sr alloy samples, indicating that the intermetallic phase was more vulnerable to

corrosion attack due to its role as the anode in galvanic corrosion.

3.2. In vitro cytocompatibility of Zn–Sr alloys

The in vitro cytocompatibility was evaluated based on cellular activity after co-culturing the MC3T3-E1 in the one-fold and two-fold diluted pure Zn and Zn-based alloy extracts for 1, 3, 5, and 7 days (Fig. 2a). Co-culturing in the one-fold diluted extract led to a significant reduction of cellular activity in pure Zn samples, while the cell activities

for the Zn-0.1Sr, Zn-0.4Sr, and Zn-0.8Sr alloy samples increased significantly. The Zn-0.8Sr extract had the largest effect on cell proliferation in comparison with the other alloys after 1 and 3 days of co-culturing. The cells co-cultured in the two-fold diluted extract exhibited a slight improvement in the pure Zn group, while the Zn-0.1Sr, Zn-0.4Sr, and Zn-0.8Sr alloy samples showed satisfactory cytocompatibility. Considering the ISO 19003-5 standard, these results indicate that pure Zn is mildly cytotoxic to MC3T3-E1 cells but Zn–Sr alloys can significantly improve cytocompatibility.
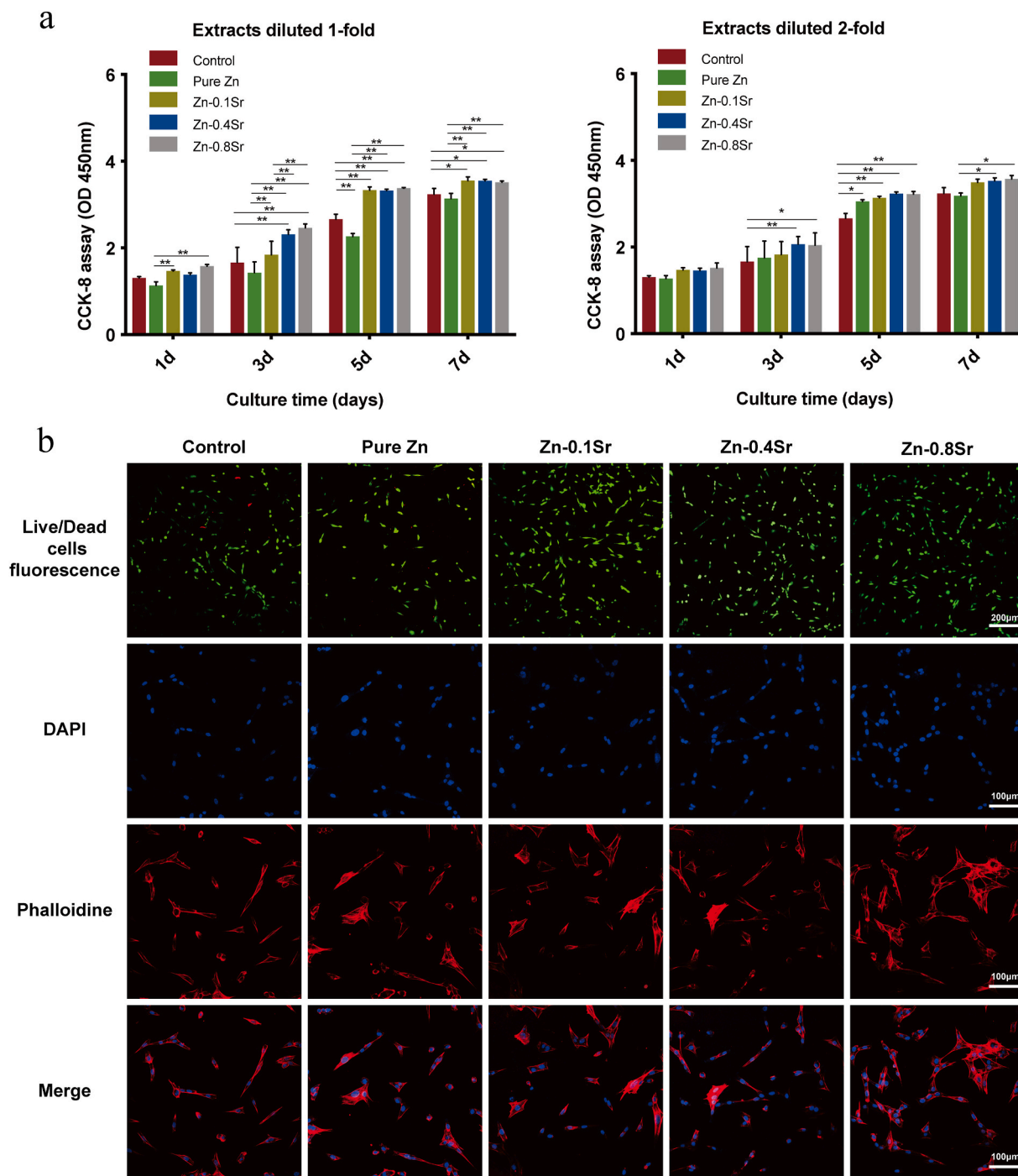
Fig. 2. In vitro cytocompatibility of Zn–Sr alloys. (a) MC3T3-E1 cell activity after co-culturing for 1, 3, 5, and 7 days in pure Zn and Zn–Sr alloy extracts (one- and two-fold dilutions; mean $\pm$ standard deviation * $p < 0.05$; **$p < 0.01$). (b) Live/dead cell staining and cytoskeletal staining of MC3T3-E1 cells cultured with pure Zn and Zn–Sr alloy extracts (one-fold dilution). Live cells were stained with green fluorescence while dead cells were stained with red fluorescence, while actin filaments were stained with phalloidin (red) and cell nuclei with DAPI (blue). (For interpretation of the references to color in this figure legend, the reader is referred to the Web version of this article.)

The influence of Zn-based alloy extracts on the viability of MC3T3-E1 cells was further verified using Live/Dead staining and cytoskeletal staining. The MC3T3-E1 cells co-cultured in the one-fold diluted Zn-based metal extracts for 3 days were stained and observed. The pure Zn group had sparse green fluorescence and low intensity in comparison with the control group (no extract), while the Zn-0.1Sr, Zn-0.4Sr, and Zn-0.8Sr groups showed significantly higher fluorescence (Fig. 2b). The cytoskeleton staining revealed that the pure Zn group underwent obvious cell shrinkage and poor cell spreading, whereas the Zn-0.1Sr, Zn-0.4Sr, and Zn-0.8Sr groups exhibited better spreading morphology, thereby demonstrating the favorable cytocompatibility of the Zn–Sr alloys.

3.3. In vitro osteogenic properties of Zn–Sr alloys

The quantitative analysis of the MC3T3-E1 cell ALP activity and osteogenic differentiation induced by the Zn-based alloy extracts is given in Fig. 3a. Osteogenic differentiation induced by exposure to a one-fold diluted Zn-based alloy extract for 7 days led to no statistically significant difference between the experimental and control groups. The Zn-0.4Sr and Zn-0.8Sr alloy groups showed relatively higher ALP activities after 14 days, while the osteogenic differentiation activity of the MC3T3-E1 cells in the pure Zn extract was inhibited. The two-fold diluted extracts led to similar results, where the Zn-0.4Sr and Zn-0.8Sr alloy extracts significantly promoted osteogenic differentiation. Overall, the Zn-0.8Sr extract led to the best results.

ALP activity staining was performed on the MC3T3-E1 cells for 14 days of induced differentiation (Fig. 3b). The Zn-0.4Sr and Zn-0.8Sr groups showed higher ALP activity than the pure Zinc and the control samples. The expression of genes related to osteogenic differentiation (ALP, COL I, OCN, Runx-2) verified these observations (Fig. 3c). The Zn–Sr alloys exhibited good osteogenic differentiation activity in vitro, where the Zn-0.8Sr alloy performed best.

3.4. Mechanism of Zn-0.8Sr alloy in promoting osteogenesis in vitro

The gene expression of the group treated with the Zn–Sr alloy extract based osteogenic media was significantly different from the group treated with the blank osteogenic medium (Fig. 4a). A comparison of the main biological functions of the up-regulated genes expressed in the Zn-0.8Sr group and the control group is given in Fig. 4b. The up-regulated expression levels of genes related to positive regulation of cell proliferation (by black underline) were linked to the improved cytocompatibility of the Zn-0.8Sr alloy in Section 3.2 (Fig. 2). Furthermore, the expression levels of genes related to bone mineralization, bone morphogenesis, ossification, and metabolic regulation of bone remodeling were significantly up-regulated (red underline), which accounted for the excellent osteogenic properties of the Zn–Sr alloys in Section 3.3 (Fig. 3). Insulin-like growth factors (IGFs) and growth factor (GF) play a crucial part in bone metabolism [36] and were up-regulated (blue underline). The genes related to the Wnt signaling pathway (green underline) are important in bone metabolism and exhibited up-regulated expression [37].

The quantitative verification results of gene expression associated with osteogenic activity are given in Fig. 4c. The expression of genes related to bone mineralization (Ibsp, Pth1r, Mmp13, Fgfr3, Pthlh, Axin2, and Aspn), bone morphogenesis (Sfrp2, Actn3, Cyp26b1, and Pappa2), ossification (Rassf2, Clec11a, Pth1r, Kazald1, Fgfr2, Fzd9, Chrdl1, Bmp4, and Mmp9), and bone remodeling regulation (Lrp5, Lepr, and Fgfr3) treated with the Zn–Sr alloy extract based osteogenic media were significantly higher than the blank control group. These results further confirmed that the Zn-0.8Sr alloy effectively promoted osteogenic differentiation by positively influencing gene expression. Several of these genes are linked to the PI3K/Akt, MAPK/Erk and Wnt signaling pathways. The activation of these signaling pathways is shown in Fig. 4d and e. The expression of Wnt3a and β-catenin was significantly higher in the

Zn-0.8Sr alloy group than those in the control group, leading to the activation of the Wnt/β-catenin signaling pathway and the slight activation of the PI3K/Akt and MAPK/Erk signaling pathways. Similarly, the increased expression of Akt and p-Akt in the Zn-0.8Sr alloy group resulted in the activation of the PI3K/Akt signaling pathway, whereas the higher expression of Erk indicates the activation of the MAPK/Erk signaling pathway in the Zn-0.8Sr alloy group. In addition, the downstream osteogenic protein expression profile indicated that the expression levels of OCN and Runx-2 were significantly higher in the Zn-0.8Sr alloy group than the control and pure Zn groups (Fig. S5).

3.5. In vivo osteogenic properties and bio-safety of Zn-0.8Sr alloy

3.5.1. Micro-CT results

The rat femoral condyle defects using the Zn-0.8Sr and Ti porous scaffolds were reconstructed using three-dimensional Micro-CT (Fig. 5a). The reconstructed images at 4, 8, and 12 weeks show the implantation position of the scaffolds, the new bone conditions, and the in vivo degradation of the Zn-0.8Sr scaffolding. The images revealed a small amount of new bone formation around the Ti and Zn-0.8Sr scaffolds (red arrow) at 4 weeks after surgery, as well as a small amount of degradation product around the Zn-0.8Sr scaffold in the form of a high-density powder-like structure (yellow arrow). A small amount of new bone tissue had developed around the Ti scaffold at 8 weeks after surgery (red arrow), while significantly more new bone tissue and thicker new trabecular structures were observed around the Zn-0.8Sr scaffold (red arrow). Furthermore, a larger amount of the degradation products had formed around the Zn-0.8Sr scaffold (yellow arrow). Larger amounts of new bone tissue surrounding the Ti and Zn-0.8Sr scaffolds were observed by 12 weeks after surgery (red arrow) in comparison with the samples observed 4 weeks after surgery. The amount of new bone increased gradually with time and was significantly higher around the Zn-0.8Sr scaffold than that around the Ti scaffold. Meanwhile, the Zn-0.8Sr alloy scaffolds gradually degraded, leading to increased amounts of surrounding degradation products (yellow arrow) and decreased scaffold volume. In addition, the quantitative analysis results in Fig. 5b further demonstrate the favorable osteogenic properties of Zn-0.8Sr alloy in vivo, as higher BMD and more new bone was found in the Zn-0.8Sr alloy group.

3.5.2. Histological analysis results

The Van Gieson staining results of the 4, 8, and 12 week postoperative samples are shown in Fig. 6a, where the dark red areas indicate regenerated bone. The full view images of the scaffolds and bone defect area confirmed that regenerative bone mass increased over time in the Zn-0.8Sr and Ti porous scaffold groups, although it was higher in the Zn-0.8Sr group. The 50 × and 100 × images revealed favorable osseointegration and bone ingrowth in both groups, but the Zn-0.8Sr scaffolds provided more space for bone ingrowth and the trabeculae of newly formed bone were thicker. The Van Gieson staining indicated that the Zn-0.8Sr scaffolds had better bone defect repair properties and favorable bone ingrowth trends. The histomorphometric analysis of both groups indicated that the bone volume fractions in the ROI increased over time (Fig. 6b). However, significantly more new bone formation was observed in the Zn-0.8Sr group than for the control group. These observations were consistent with the micro-CT results.

The toluidine blue staining shows regenerated bone as navy blue regions (Fig. 6c). Sparse new bone tissue formed around the pure Ti and Zn-0.8Sr alloy scaffolds at 4 weeks after surgery. More new bone tissue was observed around the Zn-0.8Sr alloy scaffolds at 8 weeks after surgery, while the pure Ti group barely increased. Biodegradable products were observed around the Zn-0.8Sr alloy scaffold (red arrows) by 12 weeks after surgery, and a large amount of new bone tissue was observed under low magnification (20 ×). Overall, the Zn-0.8Sr alloy scaffold exhibited significantly better bone repair effect than the pure Ti scaffold. Paragon staining was conducted using a mixture of fuchsine (basic stain)
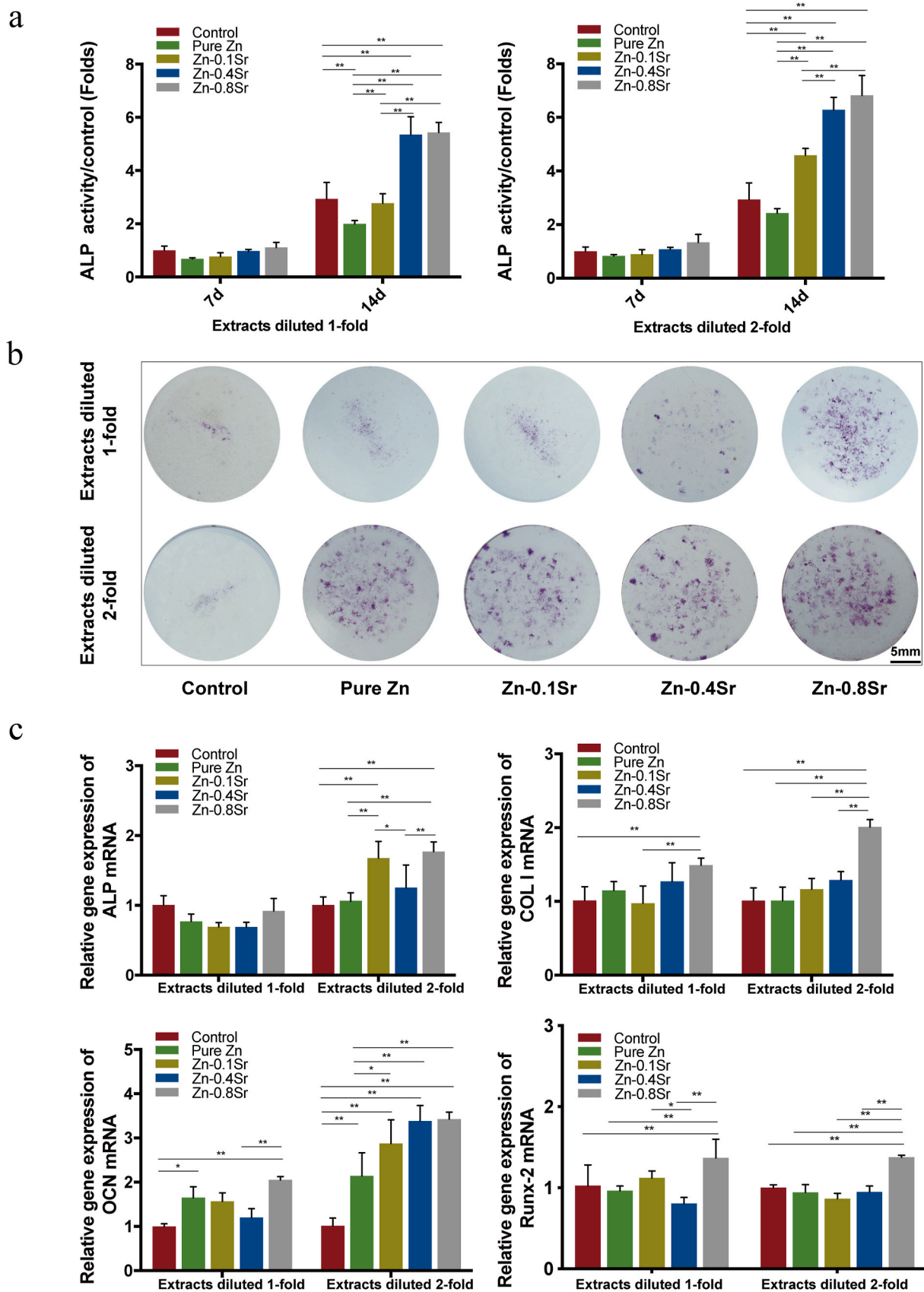
Fig. 3. In vitro osteogenesis-promoting properties of Zn–Sr alloys. (a) ALP activity, (b) ALP staining, and (c) relative expression of osteogenic differentiation marker genes in MC3T3-E1 cells cultured for the indicated times in an osteogenic medium with the pure Zn and Zn–Sr alloys extracts, given as mean ± standard deviation (*p < 0.05; **p < 0.01).
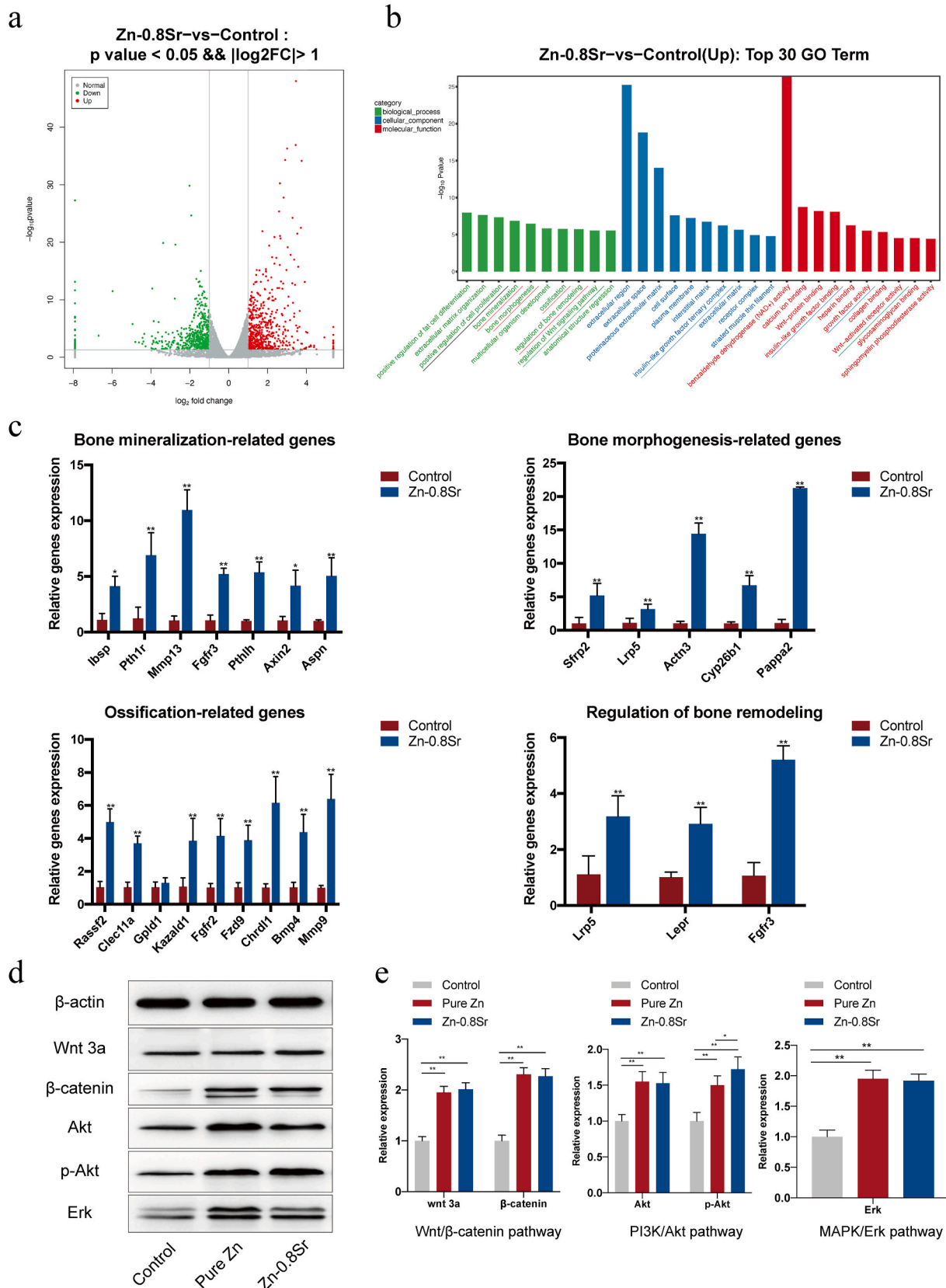
Fig. 4. RNA-sequencing and western-blot results of MC3T3-E1 cells cultured for 12 days in an Zn-0.8Sr alloy extract based osteogenic medium (two-fold dilution) and blank osteogenic medium. (a) Gene expression difference. (b) Main biological functions of the up-regulated genes. (c) Quantitative validation of gene expression related to bone mineralization, bone morphogenesis, ossification, and bone remodeling regulation. (d) Expression profile and (e) quantitative evaluation of key proteins in the PI3K/Akt, MAPK/Erk and Wnt/β-catenin signaling pathways. Data given as mean ± standard deviation. (*$p < 0.05$; **$p < 0.01$).
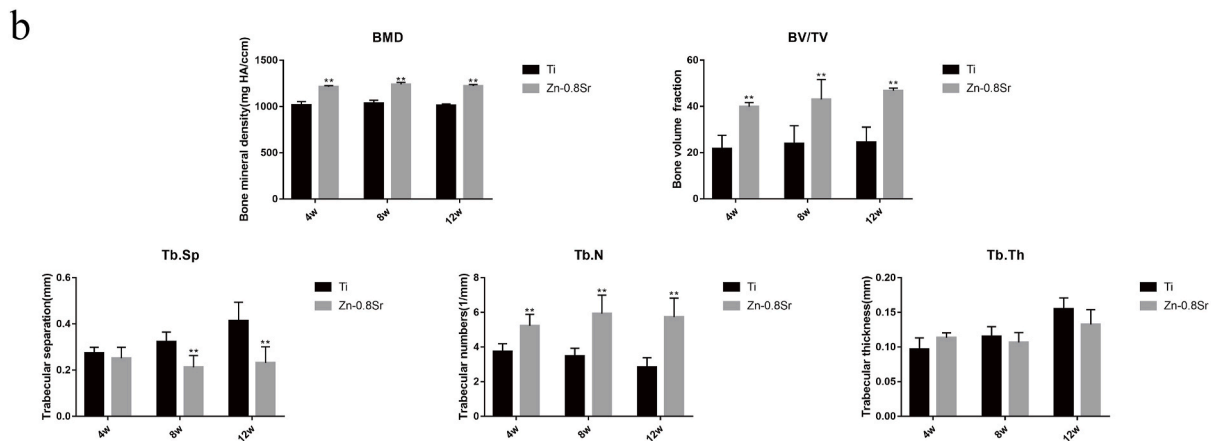
Fig. 5. Micro-CT results of in vivo bone defect repair. (a) Three-dimensional, sagittal, coronal, new bone, implants, and reconstructed micro-CT images. (b) Quantitative analyses of the osteogenesis indices, including BMD, BV/TV, Tb.N, Tb.Sp, and Tb.Th, at (left to right) 4, 8, and 12 weeks.
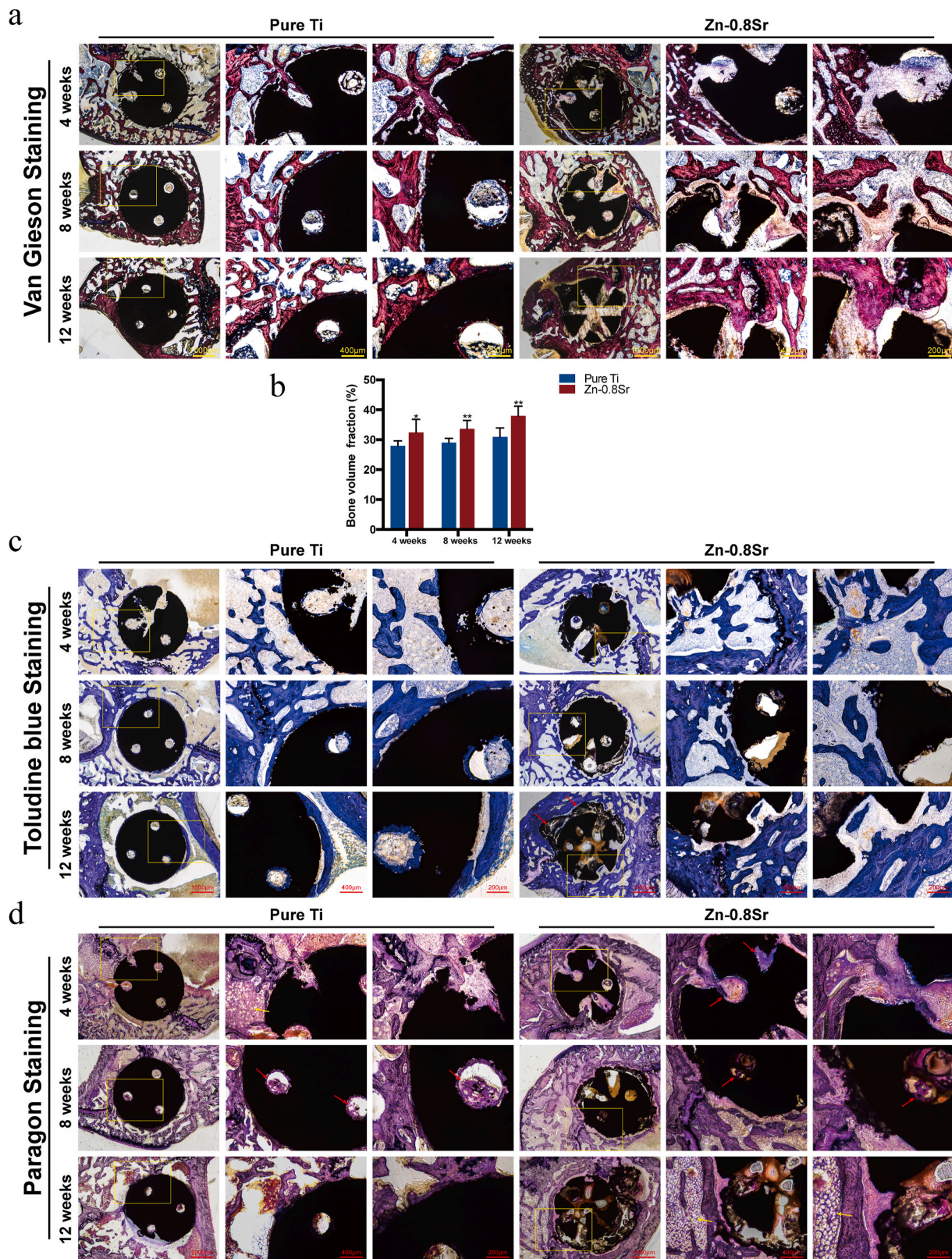
Fig. 6. Histological analysis results of the (left) pure Ti and (right) Zn-0.8Sr alloy groups. Full-view (20 ×), low-magnification (50 ×), and high-magnification (100 ×) images of the bone defect areas are arranged from left to right in each set of staining images. (a) Van Gieson staining, (b) BV/TV, (c) toluidine blue staining, where the biodegradable products of the Zn-0.8Sr alloy scaffold were observed 12 weeks after surgery (red arrows), and (d) paragon staining, where desirable bone ingrowth (red arrows), normal bone tissue morphology, regenerative bone, cartilage, and fat tissue (yellow arrows) were observed. (For interpretation of the references to color in this figure legend, the reader is referred to the Web version of this article.)

and toluidine blue (acid stain) to highlight the cellular morphology in the bone defect area in full-view images obtained under a lower magnification (20 ×) (Fig. 6d). Typical bone tissue morphology, including regenerative bone, cartilage, and fat tissue, was observed around the Ti and Zn-0.8Sr scaffolds, and no obvious inflammatory reaction was observed in either group. Exceptional bone ingrowth (red arrows) was observed under higher magnification (50 × and 100 ×). The paragon staining further validated the favorable ability of the Zn-0.8Sr alloy to promote bone regeneration and bone ingrowth, while the lack of inflammation was an indication of satisfactory biocompatibility.

3.5.3. Cross-sectional results

The SEM images and EDS mapping results of the metal implants with ambient bone tissue (red arrows) are given in Fig. 7. Samples from the pure Ti group and the Zn-0.8Sr group were harvested 12 weeks after surgery. With the exception of Ti and Zn, the main elements of the two implants, elements typically found in bone tissue, including strontium, calcium, phosphate, oxygen, and carbon, are illustrated in different colors. The EDS mapping revealed that the elements were distributed in an hierarchical structure, where three layers (bottom, middle, and top) characterized by different elemental signals were observed. Ti or Zn signals were dominant in the first layer, attributed to the main elements of the metal implants. The second layer adjacent to the implant exhibited strong C and O signals, which are the two most common elements of bio-tissue. The third layer exhibited obvious Ca and P signals, both of which are essential components of bone tissue. No degradation was observed in the cross-section of the Ti implant, but degradation products composed of Zn and O were visible in the Zn-0.8Sr implants. Moreover, the aggregation of Sr was detected in the degradation products.

3.5.4. In vivo biosafety of Zn-0.8Sr alloy

Rats from the Zn-0.8Sr alloy experimental group and the Ti control group were euthanized 12 weeks after surgery to evaluate the in vivo biosafety of the implants. H&E staining of the heart, liver, spleen, lung, and kidney tissues revealed no abnormalities or pathological morphologies in the Zn-0.8Sr alloy group in comparison with the pure Ti group
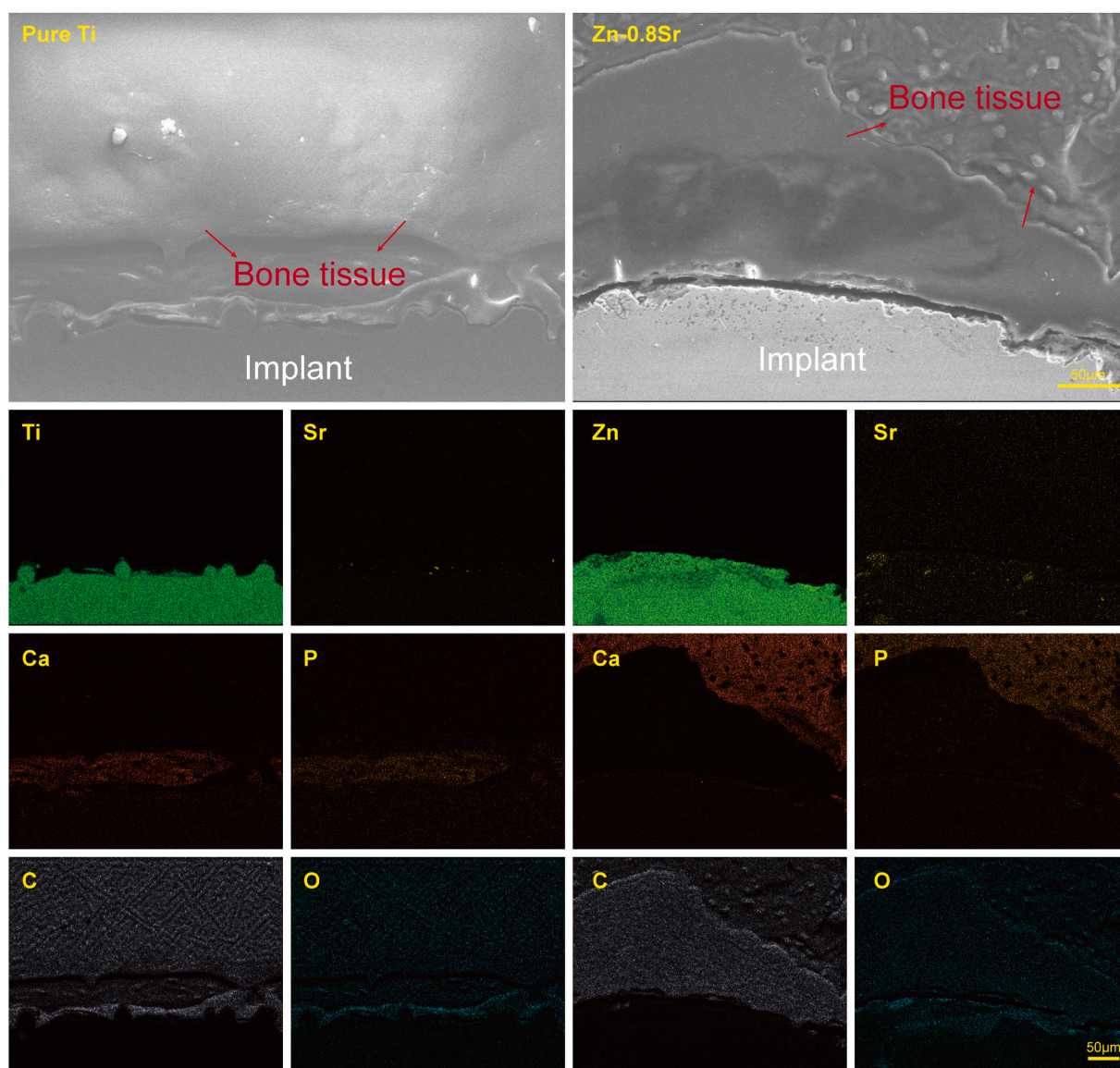
Fig. 7. EDS mapping of the pure Ti and Zn-0.8Sr alloy groups (12 weeks postoperative), where titanium (dark green), zinc (green), strontium (yellow), calcium (red), phosphate (orange), oxygen (gray), and carbon (blue) were mapped. Red arrows indicate the regeneration of bone tissue. (For interpretation of the references to color in this figure legend, the reader is referred to the Web version of this article.)
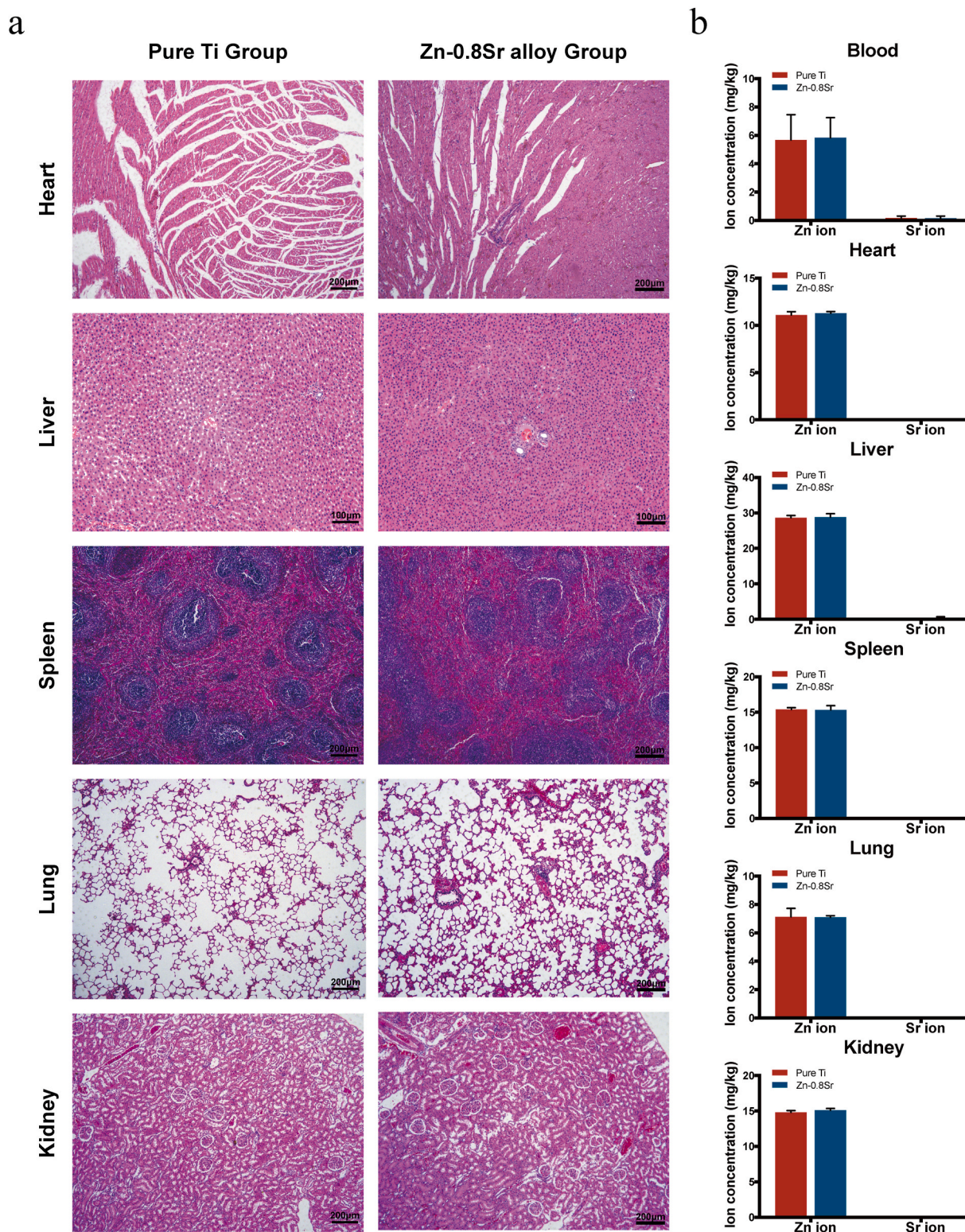
Fig. 8. In vivo biosafety of the Zn-0.8Sr alloy. (a) H&E staining of the rat heart, liver, spleen, lung, and kidney tissues from the Zn-0.8Sr alloy and pure Ti groups. (b) The concentration of Zn^{2+} and Sr^{2+} in the rat blood and organ tissues from the Zn-0.8Sr alloy and pure Ti groups.

(Fig. 8a). The concentration of Zn^{2+} and Sr^{2+} in the blood and organs of the Zn-0.8Sr group was not higher than the pure Ti implant group (Fig. 8b), indicating that the Zn-0.8Sr alloy has a relatively good in vivo biosafety and is not associated with ion accumulation within the organs.

4. Discussion

The repair of bone defects involves a series of complex and well-organized regenerative processes with distinct temporal and spatial sequences. Various cells, cytokines, and intracellular and extracellular signaling pathways participate in this process to recover normal bone

tissue function [38]. Bone tissue repair generally consists of three consecutive and overlapping stages, namely, the inflammatory stage, fibrous/bony callus stage, and bone remodeling stage [39]. The inflammatory reaction at the defect site peaks 24 h after the occurrence of the defect, where large amounts of inflammatory factors (TNF-α, IL-1, IL-6, IL-11, and IL-18) are generated [40], inflammatory cells (neutrophils and macrophages) are assembled, and damaged blood vessels secrete platelet-derived growth factor (PDGF) and transforming growth factor-b1 (TGF-b1). Simultaneously, macrophages secrete and release transforming growth factor-β (TGF-β), IGFs, and fibroblast growth factor-2 (FGF2) [41,42]. Furthermore, osteoprogenitor cells can produce BMPs. The action of all these cytokines gathers mesenchymal stem cells (MSCs). MSCs proliferate and differentiate into osteoblasts to form a fibrous callus and bony callus that is woven into the bone at the end of the callus formation [43]. Osteoblasts and osteoclasts are transformed from osteoprogenitor cells during remodeling to aid bone formation or bone resorption under the regulation of cytokines and the stimulation of strain. The woven bone is finally substituted by lamellar bone to produce a remodeled bone with fully recovered bone structure and function [44]. Effective fixation after bone injury can heal most bone injuries several months after surgery. However, 3–10% of cases exhibit delayed union or non-union, typically in those caused by severe trauma, malignant tumors, or congenital diseases [45]. Delayed union or non-union requires the application of bone repair materials, which should possess appropriate mechanical properties and several biological characteristics, namely, osteogenicity, osteoinductivity, osteoconductivity, and angiogenesis.

This study comprehensively evaluated the feasibility of Zn–Sr alloys as novel bone repair materials. The potential mechanism by which Zn–Sr alloy promoted bone regeneration is shown in Fig. 9. The biodegradable Zn–Sr alloys scaffold possessed sufficient mechanical strength for bone defect repair, even at load-bearing sites [33]. Furthermore, the
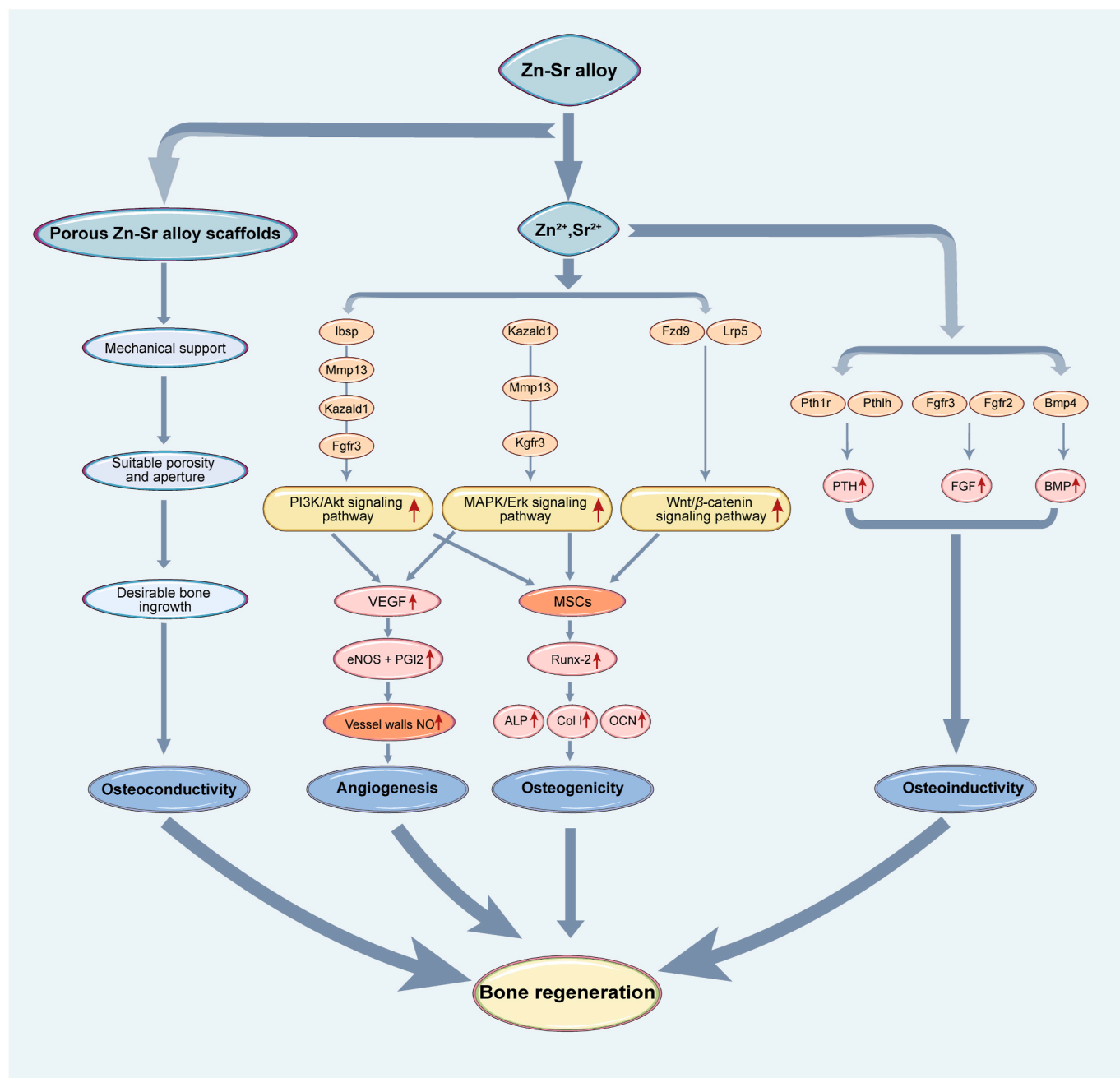
Fig. 9. A proposed mechanism through which Zn–Sr alloys promote bone regeneration.

appropriate degradation rate, aperture, and porosity provided favorable conditions for new bone ingrowth. High levels of bone ingrowth were observed within the Zn–Sr alloy scaffolds, indicating that Zn–Sr alloys offer sufficient osteoconductivity for bone repair applications (Fig. 6).

The Zn–Sr alloys exhibited satisfactory osteogenic activity in vitro and promoted bone regeneration in a rat femoral condyle defect model. The Zn–Sr alloy group had significantly better ALP activity (Fig. 3a and b), and the expression of osteogenic-related genes (ALP, COL I, OCN, and Runx-2) was significantly up-regulated (Fig. 3c). The ALP activity of the pure Zn group was slightly weaker than that of the blank control when induced in a one-fold diluted extract culture, but the Zn–Sr alloy groups exhibited better performance. The ALP activity and the expression level of osteogenesis-related genes in the pure Zn and Zn–Sr alloy groups improved significantly after being induced in a two-fold diluted extract culture, where the Zn–Sr alloys consistently performed better than pure Zn. RNA-sequencing and western-blot analysis (Fig. 4) indicated that the Zn-0.8Sr alloy activated the Wnt/β-catenin, PI3K/Akt, and MAPK/Erk signaling pathways, thereby up-regulating the expression of downstream osteogenic proteins (OCN and Runx-2) to promote osteogenesis. Runx-2 is a key regulatory factor in osteogenic differentiation that regulates the expression of many osteogenesis-related genes, including OCN, COL I, and OPN [46]. The Wnt/β-catenin signaling pathway participates throughout the bone repair process and significantly facilitates bone regeneration by promoting osteogenesis and osteoinductivity through β-catenin, regulating Runx-2, and promoting osteoblastogenesis and osteoblast function [47]. Furthermore, β-catenin plays different roles in the various bone repair processes by adjusting the ratio between osteoblasts and chondrocytes in the callus in the early stages and inducing the osteogenic differentiation of osteoblasts and osteoblastic matrix production in the later stages [37]. The PI3K/Akt and MAPK/Erk signaling pathways play crucial roles in bone repair. The PI3K/Akt signaling pathway participates in cell mitosis, thereby impacting multiple essential life processes including cell growth, survival, proliferation, and motility [48]. Therefore, the PI3K/Akt signaling pathway and downstream targets are vital for bone regeneration and bone remodeling. Activation of the PI3K/Akt signaling pathway increases the expression of OPG, Runx-2, and BMP-2 to promote the proliferation and differentiation of osteoblasts and to facilitate osteogenic activity [49]. The MAPK/Erk signaling pathway is a vital pathway between the cell surface and nucleus to regulate cell proliferation, differentiation, and death and also plays an important role in bone metabolism [50]. Activation of the MAPK/Erk signaling pathway promotes the proliferation and differentiation of osteoblasts, and the expression of osteogenesis-related genes (ALP, COL I, Runx-2 and OCN) to facilitate new bone formation [51]. The activation of MAPK/Erk and PI3K/Akt signaling pathways promoting angiogenesis by up-regulating the secretion of vascular endothelial growth factor (VEGF) via downstream signals, which promotes the release of nitric oxide (NO) in the vessel walls by up-regulating the expression of endothelial nitric oxide synthase (eNOS) and prostacyclin 2 (PGI2) [52]. Previous studies have shown that Sr ion promotes angiogenesis in vitro and in vivo [53–55], which is beneficial to bone regeneration.

The Zn-0.8Sr alloy group exhibited up-regulated expression levels of PTH-related Pth1r (parathyroid hormone 1 receptor) and Pthlh (parathyroid hormone-like peptide), FGF-related Fgfr2 (fibroblast growth factor receptor 2) and Fgfr3 (fibroblast growth factor receptor 3), and BMP-related Bmp4 (bone morphogenetic protein 4). This demonstrated the osteoinductivity of the Zn–Sr alloys, which promoted the release of essential growth factors for osteogenesis (e.g., BMP, FGF, and PTH) or enhanced their function.

The cytocompatibility and osteogenic performance of the Zn–Sr alloys was superior to the pure Zn. The Zn-0.8Sr alloy extract up-regulated the expression of key proteins (e.g., OCN and Runx-2) related to osteogenesis by activating the Wnt/β-catenin, PI3K/Akt, and MAPK/Erk signaling pathways, thereby facilitating bone regeneration. Furthermore, the activation of the PI3K/Akt and MAPK/Erk signaling pathways

could accelerate angiogenesis. However, it has not been previously established whether these effects are attributed to Zn^{2+} or Sr^{2+} alone, or whether there is a synergistic effect. There was no significant difference in the Zn^{2+} concentration in the pure Zn and Zn–Sr alloy extracts, where all ranged from 12 to 16 μg/mL (Table S2). Previous studies have reported that Zn^{2+} has a threshold effect in promoting osteoblast proliferation and differentiation, and inhibitory effects will occur at Zn^{2+} concentrations above 5.2–6.5 μg/mL [56,57]. This explains the superior cytocompatibility (Fig. 2) and osteogenic activity (Fig. 3) of the two-fold dilution (Zn^{2+} = c. 3–4 μg/mL) in comparison with the one-fold dilution (Zn^{2+} = c. 6–8 μg/mL). Despite no significant difference of Zn^{2+} concentration between the pure Zn and Zn–Sr alloy extracts, the Zn–Sr alloys groups exhibited better cytocompatibility and osteogenic activity in the one- and two-fold dilutions. The biphasic activity of Sr is similar to Zn, and its enhancement of osteoblast bone formation and inhibits osteoclast bone resorption have led to numerous studies and applications of Sr in the treatment of osteoporosis (e.g., strontium ranelate) [58]. Sr^{2+} promotes the proliferation of osteoblasts and inhibits apoptosis by activating the Akt kinase-related signaling pathway [59]. Sr^{2+} also up-regulates osteogenic differentiation by activating the RAS/MAPK signaling pathway and the downstream transcription factor Runx-2 [60]. Furthermore, it activates the MAPK/Erk [61], Wnt/β-catenin, and PI3K/Akt signaling pathways [62] by combining with the calcium-sensing receptor (CaSR) to promote bone regeneration. Sr^{2+} can down-regulate RANKL expression by increasing OPG production, which suppresses RANKL-induced osteoclastogenesis and inhibits osteoclast bone resorption [63]. The trace levels of Sr^{2+} in the Zn–Sr alloy extracts (0.98 ± 0.059 μg/mL in the Zn-0.8Sr alloy extract) and the considerable osteogenic activity of Sr^{2+} suggest that a synergistic effect between Sr^{2+} and Zn^{2+} led to improved cytocompatibility and osteogenic activity of the Zn–Sr alloys in comparison with pure Zn. Literature suggests that Sr^{2+} in Sr-containing bioceramics [64] promotes osteogenesis in the ion concentration range of 2–6 μg/mL. A bioceramic containing Sr and Si demonstrated that Sr^{2+} positively influenced osteoblast proliferation and differentiation at levels of 0.83–6.15 μg/mL, and exhibited synergistic effects with Si^{4+} to promote bone regeneration [53]. However, a lower concentration of Sr^{2+} (c. 0.25–0.5 μg/mL) exhibited favorable osteogenic activity in the current study, which is likely attributed to the presence of Zn^{2+}, which enabled Sr^{2+} to exhibit favorable osteogenic activity at a lower concentration. A previous study by the current authors observed similarities between the effects of Zn^{2+} and Sr^{2+}, where Zn^{2+} promoted osteogenesis of MSCs by activating the MAPK/Erk signaling pathway [65]. Similarly, Zn^{2+} has also been found to activate the Wnt/β-catenin [66,67] and PI3K/Akt signaling pathways [68–70]. Both Zn^{2+} and Sr^{2+} activated the Wnt/β-catenin, PI3K/Akt, and MAPK/Erk signaling pathways, which led to superior osteogenic activity of the Zn–Sr alloys compared to pure Zn. This indicated that Zn^{2+} and Sr^{2+} released during the degradation of the Zn–Sr alloys led to synergistic effects and further promoted osteogenesis. However, further research is recommended to comprehensively investigate the synergistic effects of Zn and Sr ions in facilitating osteogenesis.

5. Conclusions

Biodegradable Zn–Sr alloys exhibited satisfactory cytocompatibility in vitro. The Wnt/β-catenin, PI3K/Akt, and MAPK/Erk signaling pathways were activated by the Zn–Sr alloys. Furthermore, the alloys facilitated bone regeneration by promoting the proliferation and differentiation of MC3T3-E1 cells, up-regulating the expression of osteogenic-related genes and proteins (ALP, COL I, OCN, and Runx-2), and stimulating angiogenesis. The rat femoral condyle defect repair model confirmed the biosafety and considerable osteogenic properties of the Zn-0.8Sr alloy in vivo, which significantly promoted the bone defect repair process. The biodegradable Zn–Sr alloys exhibited the osteoconductivity, angiogenesis, osteogenecity, osteoinductivity, satisfactory mechanical properties, and biocompatibility expected of an ideal bone

repair material. These Zn–Sr alloys show great application potential to promote bone regeneration, especially in critical-sized defects on load-bearing sites.

Funding

Author contributions

Conceptualization: BJ, HTY, XHQ, YFZ, KRD; experiment data: BJ, HTY, ZCZ, XFJ, YH, QW; Formal analysis: BJ, HTY; Funding acquisition: BJ, HTY; Roles/Writing-original draft: BJ, HTY, ZCZ; Writing-review & editing: BJ, HTY, YFZ, KRD.

Declaration of competing interest

The authors declare no competing financial interests or personal relationships.

Appendix A. Supplementary data

Supplementary data to this article can be found online at https://doi.org/10.1016/j.bioactmat.2020.11.007.

References

[1] M. Montazerolghaem, A. Rasmusson, H. Melhus, H. Engqvist, M. Karlsson Ott, Simvastatin-doped pre-mixed calcium phosphate cement inhibits osteoclast differentiation and resorption, J. Mater. Sci. Mater. Med. 27 (2016) 83.

[2] M. Nabiyouni, T. Bruckner, H. Zhou, U. Gbureck, S.B. Bhaduri, Magnesium-based bioceramics in orthopedic applications, Acta Biomater. 66 (2018) 23–43.

[3] S. Ishack, A. Mediero, T. Wilder, J.L. Ricci, B.N. Cronstein, Bone regeneration in critical bone defects using three-dimensionally printed beta-tricalcium phosphate/hydroxyapatite scaffolds is enhanced by coating scaffolds with either dipyridamole or BMP-2, J. Biomed. Mater. Res. B Appl. Biomater. 105 (2017) 366–375.

[4] L. Bian, A.F.T. Mak, C. Wu, C. Cheng, Z. Gu, X. Zhang, L. Qin, A model for facilitating translational research and development in China: call for establishing a Hong Kong branch of the Chinese national engineering research centre for biomaterials, J. Orthop. Transl. 2 (2014) 170–176.

[5] J. Zhou, X. Guo, Q. Zheng, Y. Wu, F. Cui, B. Wu, Improving osteogenesis of three-dimensional porous scaffold based on mineralized recombinant human-like collagen via mussel-inspired polydopamine and effective immobilization of BMP-2-derived peptide, Colloids Surf. B Biointerfaces 152 (2017) 124–132.

[6] M.J. Webber, E.A. Appel, E.W. Meijer, R. Langer, Supramolecular biomaterials, Nat. Mater. 15 (2015) 13–26.

[7] C. Dellavia, M. Giammattei, D. Carmagnola, F. Musto, E. Canciani, M. Chiapasco, Iliac crest fresh-frozen allografts versus autografts in oral pre-prosthetic bone reconstructive surgery: histologic and histomorphometric study, Implant Dent. 25 (2016) 731–738.

[8] C.M. Rice, E.A. Mallam, A.L. Whone, P. Walsh, D.J. Brooks, N. Kane, S.R. Butler, D. I. Marks, N.J. Scolding, Safety and feasibility of autologous bone marrow cellular therapy in relapsing-progressive multiple sclerosis, Clin. Pharmacol. Ther. 87 (2010) 679–685.

[9] D. He, P. Liu, X. Liu, X. Chen, F. Ma, W. Li, C. Zhao, J. Tu, Hydroxyapatite bioceramic coatings prepared by hydrothermal-electrochemical deposition method, J. Wuhan Univ. Technol.-Materials Sci. Ed. 29 (2014) 398–400.

[10] Y.F. Zheng, X.N. Gu, F. Witte, Biodegradable metals, Mater. Sci. Eng. R Rep. 77 (2014) 1–34.

[11] K. Glenske, P. Donkiewicz, A. Kowitsch, N. Milosevic-Oljaca, P. Rider, S. Rofall, J. Franke, O. Jung, R. Smeets, R. Schnettler, S. Wenisch, M. Barbeck, Applications of metals for bone regeneration, Int. J. Mol. Sci. 19 (2018) 826.

[12] H.A. Ching, D. Choudhury, M.J. Nine, N.A. Abu Osman, Effects of surface coating on reducing friction and wear of orthopaedic implants, Sci. Technol. Adv. Mater. 15 (2014), 014402.

[13] Z. Li, P. Munroe, Z.-t. Jiang, X. Zhao, J. Xu, Z.-f. Zhou, J.-q. Jiang, F. Fang, Z.-h. Xie, Designing superhard, self-toughening CrAlN coatings through grain boundary engineering, Acta Mater. 60 (2012) 5735–5744.

[14] T.W. Bauer, G.F. Muschler, Bone graft materials. An overview of the basic science, Clin. Orthop. Relat. Res. 371 (2000) 10–27.

[15] W.C. Pederson, D.W. Person, Long bone reconstruction with vascularized bone grafts, Orthop. Clin. 38 (2007) 23–35.

[16] X. Tong, D. Zhang, X. Zhang, Y. Su, Z. Shi, K. Wang, J. Lin, Y. Li, J. Lin, C. Wen, Microstructure, mechanical properties, biocompatibility, and in vitro corrosion and degradation behavior of a new Zn-5Ge alloy for biodegradable implant materials, Acta Biomater. 82 (2018) 197–204.

[17] A. Kafri, S. Ovadia, G. Yosafovich-Doitch, E. Aghion, The effects of 4%Fe on the performance of pure zinc as biodegradable implant material, Ann. Biomed. Eng. 47 (2019) 1400–1408.

[18] X. Qu, H. Yang, Z. Yu, B. Jia, H. Qiao, Y. Zheng, K. Dai, Serum zinc levels and multiple health outcomes: implications for zinc-based biomaterials, Bioact. Mater. 5 (2020) 410–422.

[19] K.A. McCall, C. Huang, C.A. Fierke, Function and mechanism of zinc metalloenzymes, J. Nutr. 130 (2000) 1437S–1446S.

[20] M. Yamaguchi, Role of nutritional zinc in the prevention of osteoporosis, Mol. Cell. Biochem. 338 (1–2) (2010) 241–254.

[21] M. Yamaguchi, H. Oishi, Y. Suketa, Stimulatory effect of zinc on bone formation in tissue culture, Biochem. Pharmacol. 36 (1987) 4007–4012.

[22] D. Chen, L.C. Waite, W.M. Pierce Jr., In vitro effects of zinc on markers of bone formation, Biol. Trace Elem. Res. 68 (1999) 225–234.

[23] M. Yamaguchi, T. Matsui, Stimulatory effect of zinc-chelating dipeptide on deoxyribonucleic acid synthesis in osteoblastic MC3T3-E1 cells, Peptides 17 (1996) 1207–1211.

[24] X. Fu, Y. Li, T. Huang, Z. Yu, K. Ma, M. Yang, Q. Liu, H. Pan, H. Wang, J. Wang, M. Guan, Runx2/Osterix and zinc uptake synergize to orchestrate osteogenic differentiation and citrate containing bone apatite formation, Adv. Sci. 5 (2018) 1700755.

[25] H.J. Seo, Y.E. Cho, T. Kim, H.I. Shin, I.S. Kwun, Zinc may increase bone formation through stimulating cell proliferation, alkaline phosphatase activity and collagen synthesis in osteoblastic MC3T3-E1 cells, Nutr. Res. Pract. 4 (2010) 356–361.

[26] K. Yusa, O. Yamamoto, M. Fukuda, S. Koyota, Y. Koizumi, T. Sugiyama, In vitro prominent bone regeneration by release zinc ion from Zn-modified implant, Biochem. Biophys. Res. Commun. 412 (2011) 273–278.

[27] P.K. Bowen, J. Drelich, J. Goldman, Zinc exhibits ideal physiological corrosion behavior for bioabsorbable stents, Adv. Mater. 25 (2013) 2577–2582.

[28] H. Yang, X. Qu, W. Lin, C. Wang, D. Zhu, K. Dai, Y. Zheng, In vitro and in vivo studies on zinc-hydroxyapatite composites as novel biodegradable metal matrix composite for orthopedic applications, Acta Biomater. 71 (2018) 200–214.

[29] J. Li, S. Xiang, H. Luan, A. Amar, X. Liu, S. Lu, Y. Zeng, G. Le, X. Wang, F. Qu, C. Jiang, G. Yang, Additive manufacturing of high-strength CrMnFeCoNi high-entropy alloys-based composites with WC addition, J. Mater. Sci. Technol. 35 (2019) 2430–2434.

[30] S. Chao, X. Liu, F. Bo, P. Lan, F.Y. Zhou, X. Li, H. Wang, X. Xin, L. Li, Z. Shen, Mechanical properties: in vitro degradation behavior, hemocompatibility and cytotoxicity evaluation of Zn-1.2Mg alloy for biodegradable implants, RSC Adv. 6 (2016) 86410–86419.

[31] H.F. Li, X.H. Xie, Y.F. Zheng, Y. Cong, F.Y. Zhou, K.J. Qiu, X. Wang, S.H. Chen, L. Huang, L. Tian, L. Qin, Development of biodegradable Zn-1X binary alloys with nutrient alloying elements Mg, Ca and Sr, Sci. Rep. 5 (2015) 10719.

[32] B. Jia, H. Yang, Y. Han, Z. Zhang, X. Qu, Y. Zhuang, Q. Wu, Y. Zheng, K. Dai, In vitro and in vivo studies of Zn-Mn biodegradable metals designed for orthopedic applications, Acta Biomater. 108 (2020) 358–372.

[33] H. Yang, B. Jia, Z. Zhang, X. Qu, G. Li, W. Lin, D. Zhu, K. Dai, Y. Zheng, Alloying design of biodegradable zinc as promising bone implants for load-bearing applications, Nat. Commun. 11 (2020) 401.

[34] L.-L. Zhu, S. Zaidi, Y. Peng, H. Zhou, B.S. Moonga, A. Blesius, I. Dupin-Roger, M. Zaidi, L. Sun, Induction of a program gene expression during osteoblast differentiation with strontium ranelate, Biochem. Biophys. Res. Commun. 355 (2007) 307–311.

[35] H. Yang, X. Qu, W. Lin, D. Chen, D. Zhu, K. Dai, Y. Zheng, Enhanced osseointegration of Zn-Mg composites by tuning the release of Zn ions with sacrificial Mg-rich anode design, ACS Biomater. Sci. Eng. 5 (2018) 453–467.

[36] R. Dimitriou, E. Tsiridis, P.V. Giannoudis, Current concepts of molecular aspects of bone healing, Injury 36 (2005) 1392–1404.

[37] K.S. Houschyar, C. Tapking, M.R. Borrelli, D. Popp, D. Duscher, Z.N. Maan, M. P. Chelliah, J. Li, K. Harati, C. Wallner, S. Rein, D. Pforringer, G. Reumuth, G. Grieb, S. Mouraret, M. Dadras, J.M. Wagner, J.Y. Cha, F. Siemers, M. Lehnhardt, B. Behr, Wnt pathway in bone repair and regeneration – what do we know so far, Front. Cell Dev. Biol. 6 (2018) 170.

[38] T.J. Cho, L.C. Gerstenfeld, T.A. Einhorn, Differential temporal expression of members of the transforming growth factor beta superfamily during murine fracture healing, J. Bone Miner. Res. 17 (2002) 513–520.

[39] X. Wang, Y. Wang, W. Gou, Q. Lu, J. Peng, S. Lu, Role of mesenchymal stem cells in bone regeneration and fracture repair: a review, Int. Orthop. 37 (2013) 2491–2498.

[40] N.L. Fazzalari, Bone fracture and bone fracture repair, Osteoporos. Int. 22 (2011) 2003–2006.

[41] J.R. Lieberman, A. Daluiski, T.A. Einhorn, The role of growth factors in the repair of bone, J. Bone Joint Surg. 84 (2002) 1032–1044.

[42] T.J. Cho, L.C. Gerstenfeld, T.A. Einhorn, Differential temporal expression of members of the transforming growth factor β superfamily during murine fracture healing, J. Bone Joint Surg. 17 (2002) 513–520.

[43] H.C. Fayaz, P.V. Giannoudis, M.S. Vrahas, R.M. Smith, C. Moran, H.C. Pape, C. Krettek, J.B. Jupiter, The Role of Stem Cells in Fracture Healing and Nonunion, vol. 35, 2011, pp. 1587–1597.

[44] R. Marsell, T.A. Einhorn, The biology of fracture healing, Injury 42 (2011) 551–555.

[45] P. Kloen, G.A. Buijze, D. Ring, Management of forearm nonunions: current concepts, Strat, Trauma Limb Reconstr 7 (2012) 1–11.

[46] P. Ducy, R. Zhang, V. Geoffroy, A.L. Ridall, G. Karsenty, Osf2/Cbfa1: a transcriptional activator of osteoblast differentiation, Cell 89 (1997) 747–754.

[47] Venkatesh Krishnan, Regulation of bone mass by Wnt signaling, J. Clin. Invest. 116 (2006) 1202–1209.

[48] M. Martini, M.C. De Santis, L. Braccini, F. Gulluni, E. Hirsch, PI3K/AKT signaling pathway and cancer: an updated review, Ann. Med. 46 (2014) 372–383.

[49] M. Majidinia, A. Sadeghpour, B. Yousefi, The roles of signaling pathways in bone repair and regeneration, J. Cell. Physiol. 233 (2018) 2937–2948.

[50] C. Ge, G. Xiao, D. Jiang, R.T. Franceschi, Critical role of the extracellular signal-regulated kinase-MAPK pathway in osteoblast differentiation and skeletal development, J. Cell Biol. 176 709-718.

[51] W. Gong, Y. Dong, S. Wang, X. Gao, X. Chen, A novel nano-sized bioactive glass stimulates osteogenesis via the MAPK pathway, RSC Adv. 7 (2017) 13760–13767.

[52] M. Rajabi, S.A. Mousa, The role of angiogenesis in cancer treatment, Biomedicines 5 (2017) 34.

[53] L. Mao, L. Xia, J. Chang, J. Liu, L. Jiang, C. Wu, B. Fang, The synergistic effects of Sr and Si bioactive ions on osteogenesis, osteoclastogenesis and angiogenesis for osteoporotic bone regeneration, Acta Biomater. 61 (2017) 217–232.

[54] K. Lin, P. Liu, L. Wei, Z. Zou, W. Zhang, Y. Qian, Y. Shen, J. Chang, Strontium substituted hydroxyapatite porous microspheres: surfactant-free hydrothermal synthesis, enhanced biological response and sustained drug release, Chem. Eng. J. 222 (2013) 49–59.

[55] W. Zhang, H. Cao, X. Zhang, G. Li, Q. Chang, J. Zhao, Y. Qiao, X. Ding, G. Yang, X. Liu, X. Jiang, A strontium-incorporated nanoporous titanium implant surface for rapid osseointegration, Nanoscale 8 (2016) 5291–5301.

[56] J. Ma, N. Zhao, D. Zhu, Endothelial cellular responses to biodegradable metal zinc, ACS Biomater. Sci. Eng. 1 (2015) 1174–1182.

[57] M. Yamaguchi, A. Igarashi, S. Uchiyama, Bioavailability of zinc yeast in rats: stimulatory effect on bone calcification in vivo, J. Health Sci. 50 (2004) 75–81.

[58] R.D. Prabha, B.P. Nair, N. Ditzel, J. Kjems, P.D. Nair, M. Kassem, Strontium functionalized scaffold for bone tissue engineering, Mater. Sci. Eng. C Mater. Biol. Appl. 94 (2019) 509–515.

[59] M.S. Rybchyn, M. Slater, A.D. Conigrave, R.S. Mason, An Akt-dependent increase in canonical Wnt signaling and a decrease in sclerostin protein levels are involved in strontium ranelate-induced osteogenic effects in human osteoblasts, J. Biol. Chem. 286 (2011) 23771–23779.

[60] S. Peng, G. Zhou, K.D.K. Luk, K.M.C. Cheung, Z. Li, W.M. Lam, Z. Zhou, W.W. Lu, Strontium promotes osteogenic differentiation of mesenchymal stem cells through the Ras/MAPK signaling pathway, Cell. Physiol. Biochem. 23 (2009) 165–174.

[61] Z. Saidak, P.J. Marie, Strontium signaling: molecular mechanisms and therapeutic implications in osteoporosis, Pharmacol. Ther. 136 (2012) 216–226.

[62] W. Zhang, Y. Tian, H. He, R. Chen, Y. Ma, H. Guo, Y. Yuan, C. Liu, Strontium attenuates rhBMP-2-induced osteogenic differentiation via formation of Sr-rhBMP-2 complex and suppression of Smad-dependent signaling pathway, Acta Biomater. 33 (2016) 290–300.

[63] G.A. Fielding, W. Smoot, S. Bose, Effects of SiO2, SrO, MgO, and ZnO dopants in tricalcium phosphates on osteoblastic Runx2 expression, J. Biomed. Mater. Res. 102 (2014) 2417–2426.

[64] P. Naruphontjirakul, A.E. Porter, J.R. Jones, In vitro osteogenesis by intracellular uptake of strontium containing bioactive glass nanoparticles, Acta Biomater. 66 (2018) 67–80.

[65] D. Zhu, Y. Su, M.L. Young, J. Ma, Y. Zheng, L. Tang, Biological responses and mechanisms of human bone marrow mesenchymal stem cells to Zn and Mg biomaterials, ACS Appl. Mater. Interfaces 9 (2017) 27453–27461.

[66] J.Y. Zhou, H.L. Lin, Z. Wang, S.W. Zhang, D.G. Huang, C.Q. Gao, H.C. Yan, X.Q. Wang, Zinc L-aspartate enhances intestinal stem cell activity to protect the integrity of the intestinal mucosa against deoxynivalenol through activation of the Wnt/β-catenin signaling pathway, Environ. Pollut. 262 (2020) 114290.

[67] J. Zhang, Y.D. Park, W.J. Bae, A. El-Fiqi, S.H. Shin, E.J. Lee, H.W. Kim, E.C. Kim, Effects of bioactive cements incorporating zinc-bioglass nanoparticles on odontogenic and angiogenic potential of human dental pulp cells, J. Biomater. Appl. 29 (2015) 954–964.

[68] X. Zhang, D. Liang, J. Fan, X. Lian, Y. Zhao, X. Wang, Z.H. Chi, P. Zhang, Zinc attenuates tubulointerstitial fibrosis in diabetic nephropathy via inhibition of HIF through PI-3K signaling, Biol. Trace Elem. Res. 173 (2016) 372–383.

[69] X. Dong, S. Tang, W. Zhang, W. Gao, Y. Chen, GPR39 activates proliferation and differentiation of porcine intramuscular preadipocytes through targeting the PI3K/AKT cell signaling pathway, J. Recept. Signal Transduct. Res. 36 (2016) 130–138.

[70] G. Akbari, Role of zinc supplementation on ischemia/reperfusion injury in various organs, Biol. Trace Elem. Res. 196 (2020) 1–9.